Dynamic Modeling of Soot Particle Coagulation and Aggregation: Implementation With the Method of Moments and Application to High-Pressure Laminar Premixed Flames

ANDREI KAZAKOV

Engine Research Center, Department of Mechanical Engineering, University of Wisconsin-Madison, Madison, WI 53706

and

MICHAEL FRENKLACH*

Department of Mechanical Engineering, University of California at Berkeley, Berkeley, CA 94720-1740

The method of moments was extended to include a more complete description of particle coagulation, namely, the transition and continuum regimes as well as the formation and growth of fractal aggregates. The formalism preserves the numerical efficiency and the physical rigor of the method of moments by inclusion of just two additional moment equations and without prescribing a mathematical form to the particle size distribution function. The extended model was used to simulate soot formation in several 10 bar laminar premixed ethylene-air flames. The results demonstrate that the more complete formulation improves significantly model prediction of experimental data, thereby explaining the appearance of a catastrophic decrease in coagulation rates, which could not be rationalized within the classical theory of Brownian coagulation. © 1998 by The Combustion Institute

INTRODUCTION

Detailed modeling of soot formation has advanced in recent years to a degree that comparison with experiment has become quantitative [1–6]. In pursuing these developments, the main focus was on the initial phases of particle inception and on experimental data collected in laminar premixed flames at atmospheric and subatmospheric pressures. For such conditions, the assumptions of the free-molecular regime of particle coagulation and the spherical shape of soot particles were reasonable. At elevated pressures, those of interest to modeling practical combustion, the mean free path decreases and coagulation switches to the transition and continuum regimes. In addition, soot particles agglomerate into fractal aggregates, becoming more pronounced with the increase in gas density or carbon content. The objective of the present work is to consider both of these factors for detailed modeling of soot formation.

The dynamics of coagulation is fundamentally described by the Smoluchowski master equations [7], an infinite number of differential equations describing the population of different size particles [8]. Analytical solutions are possible only for unrealistically idealized cases (see [9] and references therein) and the direct numerical integration is computationally so intensive [10, 11] that its utilization in combustion modeling is impractical. The most efficient way of numerical solution is a method moments, which reformulates the problem into a small set of differential equations describing evolution of moments of the particle size distribution function (PSDF). A variation of this method [10], which requires no a priori knowledge of PSDF as most of such methods do, has been employed by us [1–3, 12, 13] and others [5, 6] for modeling soot formation. That formulation [10, 12] was developed for the free-molecular regime of coagulation. The present work extends this formulation to include the transition and continuum regimes, as well as the formation and growth of fractal aggregates.

The extended model was then used to simulate several 10 bar laminar premixed ethylene-air flames of Bönig et al. [14] examined by us recently [3]. We investigated the differences introduced by the more complete description of coagulation and showed that such complete

---

*Corresponding author.

treatment explains the unusual behavior reported by Feldermann et al. [15], who observed that in the post-flame zone of high-pressure laminar premixed flames soot particle number density remains nearly constant, whereas the classical theory of Brownian coagulation [8, 16, 17] predicts its monotonic decrease.

MODEL DEVELOPMENT

The Method of Moments

The following summarizes the key elements of the method of moments, those essential to the presentation of the new development. For a complete description the reader is referred to [1, 10, 18].

The dynamics of particle coagulation can be described by the following set of equations

$$\frac{dM_0}{dt} = R_0 - G_0, \tag{1.0}$$

$$\frac{dM_1}{dt} = R_1 + W_1, \tag{1.1}$$

$$\frac{dM_2}{dt} = R_2 + G_2 + W_2, \tag{1.2}$$

$\cdots$

$$\frac{dM_r}{dt} = R_r + G_r + W_r, \tag{1.r}$$

where R, G, and W are the nucleation, coagulation, and surface growth terms, respectively;

$$M_r = \sum_{i=1}^{\infty} m_i^r N_i, \tag{2}$$

$$\mu_r = M_r/M_0, \tag{3}$$

are the rth concentration and size PSDF moments, respectively; m_i and N_i are the mass and number density, respectively, of particles of size class i; and t is the reaction time. As before, a five-moment model (i.e., up to $r = 5$) was employed in the present study.

The nucleation terms R in Eqs. 1 are specified by the preparticle chemistry and the surface growth terms by

$$W_r = k_s C_g \alpha \chi_s \sum_{i=1}^{\infty} \sum_{k=0}^{r-1} \binom{r}{k} m_i^k \Delta^{r-k} S_i N_i, \tag{4}$$

where k_s is the per-site rate coefficient; C_g the concentration of a gaseous species; α the fraction of surface sites available for reaction; χ_s the nominal number density of surface sites; Δ the change of mass in a single reaction event; and m_i, S_i, and N_i are the mass, surface area, and number density of the ith particle, respectively. The coagulation terms in Eqs. 1 are defined as

$$G_0 = \frac{1}{2} \sum_{i=1}^{\infty} \sum_{j=1}^{\infty} \beta_{ij} N_i N_j, \tag{5.0}$$

$$G_r = \frac{1}{2} \sum_{k=1}^{r-1} \binom{r}{k} \left(\sum_{i=1}^{\infty} \sum_{j=1}^{\infty} m_i^k m_j^{r-k} \beta_{ij} N_i N_j \right),$$

$$r = 2, 3, \cdots, \tag{5.r}$$

where β_{ij} is the collision frequency; its functional form depends on coagulation regime.

Complete Description of Particle Coagulation

Particle coagulation is classified on the basis of the Knudsen number, Kn $= 2\lambda/d$, where λ is the gas mean free path and d the particle diameter [8]. The free molecular coagulation is characterized by Kn $\gg 1$ [8]. We have expressed the collision frequency of soot particles in this regime as [12]

$$\beta_{ij}^f = 2.2 \sqrt{\frac{6 k_B T}{\rho}} \left(\frac{3 m_C}{4 \pi \rho} \right)^{1/6} \sqrt{\frac{1}{m_i} + \frac{1}{m_j}} (m_i^{1/3}$$

$$+ m_j^{1/3})^2, \tag{6}$$

where k_B is the Boltzmann constant; T is the temperature; ρ is the density of soot particle material, assumed equal 1.8 g/cm^3; m is the particle mass in the units of carbon atoms; m_C is the mass of a carbon atom; and the multiplier 2.2 is the van der Waals enhancement factor [19]. Equations 1 are solved using a double interpolation scheme among moments [10] with the details summarized in [10, 12].

The same numerical approach can be applied [10] to the other limit, Kn $\ll 1$, the continuum regime of coagulation. In this limit, the collision frequency is given by [8, 20]

TABLE 1

Particle Size Distribution Functions Used for the Numerical Tests of Eq. 9

Name	$f(z)$	Parameter	Maximum relative error (%)		
			G_0	G_1	G_2
Monodisperse	1 at $z = z_0$, 0 otherwise		14	14	14
Uniform	$1/z_0$ at $z < z_0$, 0 otherwise		18	18	18
Exponential	$z_0^{-1} \exp(-z/z_0)$		18	18	18
Lognormal	$1/(3z\sqrt{2\pi} \log \sigma)$ $\exp(-[\log^2 (z/z_0)]/[18 \log^2 \sigma])$	$\sigma = 1.26 - 2.28$	18	18	25
Gamma[a]	$1/[z_0\Gamma(p)](z/z_0)^{p-1}$ $\exp(-[z/z_0])$	$p = 2, 3$	17	17	17
Weibull[a]	$1/[z_0 p\Gamma(p)] (z/z_0)^{p-1}$ $\exp[-(z/z_0)^p]$	$p = 1.5, 2$	18	18	18

[a] Notation Γ stands for the gamma function.

$$\beta_{ij}^c = K\left(\frac{C_i}{m_i^{1/3}} + \frac{C_j}{m_j^{1/3}}\right)(m_i^{1/3} + m_j^{1/3}), \qquad (7)$$

where $K = 2k_{\mathrm{B}}T/3\eta$, η is gas viscosity, and C the Cunningham slip correction factor. We expressed the latter in the form $C = 1 + 1.257$ Kn [20, 21]. No van der Waals enhancement is included in Eq. 7; this follows the numerical results of Harris and Kennedy [11], which showed that the collision enhancement at high pressures is relatively small. Substitution of Eq. 7 into Eqs. 5 results in

$$G_0^c = K\Big[1 + \mu_{1/3}\mu_{-1/3}$$

$$+ 2.514\lambda\left(\frac{\pi\rho}{6m_C}\right)^{1/3}(\mu_{-1/3}$$

$$+ \mu_{1/3}\mu_{-2/3})\Big]M_0^2 \qquad (8.0)$$

$$G_r^c = \frac{1}{2}K \sum_{k=1}^{r-1} \binom{r}{k}\Big[2\mu_k\mu_{r-k} + \mu_{k+1/3}\mu_{r-k-1/3}$$

$$+ \mu_{k-1/3}\mu_{r-k+1/3}$$

$$+ 2.514\lambda\left(\frac{\pi\rho}{6m_C}\right)^{1/3}(\mu_{k-1/3}\mu_{r-k}$$

$$+ \mu_k\mu_{r-k-1/3} + \mu_{k+1/3}\mu_{r-k-2/3}$$

$$+ \mu_{k-2/3}\mu_{r-k+1/3})\Big]M_0^2 \qquad (8.r)$$

for $r = 1, 2, \cdots$. The fractional-order moments appearing in these equations were evaluated by interpolation among whole-order moments determined through solution of Eqs. 1.

Coagulation in between the two limits is referred to as the transition regime. The collision frequency in this regime is usually expressed by the semiempirical formula of Fuchs [16]. The functional form of this expression is rather complex for implementation with the method of moments. Pratsinis [21] suggested to approximate the coagulation rate in the transition regime with the harmonic mean of the limit values, i.e.,

$$G_r = \frac{G_r^f G_r^c}{G_r^f + G_r^c}, r = 0, 2, 3,\cdots, \qquad (9)$$

where superscripts f and c refer to the free-molecular and continuum regimes, respectively. A similar approach was used by Mackowski et al. [22]. Equation 9 was shown [21] to reproduce the formula of Fuchs within 14%. However, this assessment was made with a monodispersed PSDF. Our calculations confirmed Pratsinis' result for the monodispersed case (shown in Table 1 and Fig. 1), and we extended the numerical testing of Eq. 9 to a wide range of particle size distributions.

To account for the properties of the surrounding gas in a convenient manner, Fuchs' coagulation formula [8, 16] was rewritten in a dimensionless form
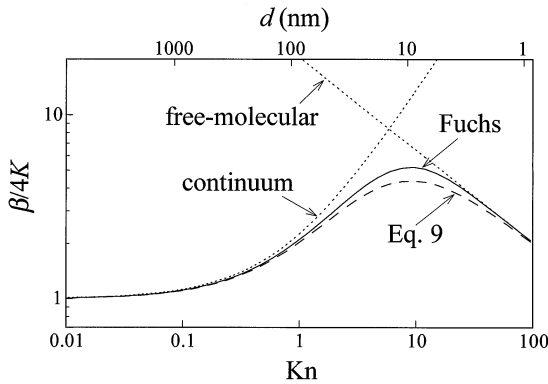
Fig. 1. Collision frequency calculated for equal-sized soot particles with different analytical expressions at a pressure of 10 bar and a temperature of 1800 K.
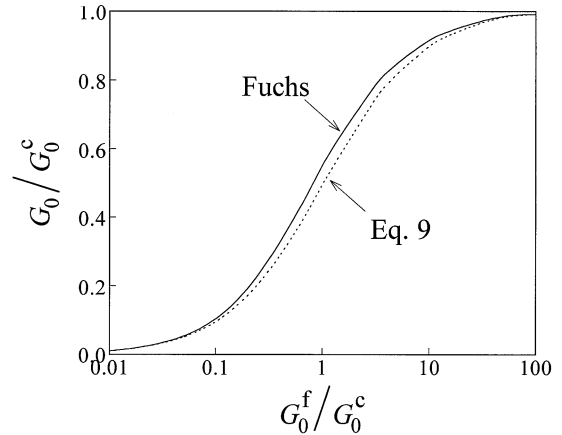

Fig. 2. Transition from the free-molecular to continuum regime of particle coagulation calculated for an exponential PSDF with $z_0 = 1$ (see Table 1); solid line represents the Fuchs formula, Eq. 10, and dotted line the harmonic-mean approximation, Eq. 9.

$$\tilde{\beta}_{ij} = \beta_{ij}/K$$

$$= \tilde{\beta}_{ij}^{c}\left[\frac{z_i^{1/3} + z_j^{1/3}}{z_i^{1/3} + z_j^{1/3} + 2(\tilde{\delta}_i^2 + \tilde{\delta}_j^2)^{1/2}} + \zeta\,\frac{\tilde{\beta}_{ij}^{c}}{\tilde{\beta}_{ij}^{f}}\right]^{-1},$$

$$(10)$$

where

$$z = \mathrm{Kn}^{-3},$$

$$\zeta = \frac{1}{3\eta}\,\sqrt{\frac{2k_{\mathrm{B}}T\rho}{3\lambda}},$$

$$\tilde{\delta} = z^{1/3}\left[\frac{(1 + X)^3 - (1 + X^2)^{3/2}}{3X^2} - 1\right],$$

$$X = \frac{\pi z^{1/6}}{\zeta C},$$

$$\tilde{\beta}_{ij}^{f} = \beta_{ij}^{f}\zeta/K = \sqrt{\frac{1}{z_i} + \frac{1}{z_j}}\,(z_i^{1/3} + z_j^{1/3})^2, \qquad (6')$$

$$\tilde{\beta}_{ij}^{c} = \beta_{ij}^{c}/K = (z_i^{1/3} + z_j^{1/3})\left(\frac{C_i}{z_i^{1/3}} + \frac{C_j}{z_j^{1/3}}\right). \qquad (7')$$

In this formulation, variable z represents the dimensionless mass of a colliding particle and parameter ζ combines the properties of the surrounding medium as well as the density of particle material. Superscripts f and c, as before, refer to the free-molecular and continuum regimes, respectively.

The initial series of numerical tests was performed with several types of PSDF, those commonly used for aerosol characterization; these functions, along with the results obtained, are listed in Table 1. The tests were designed to cover a wide range of physical conditions. Within each class of PSDF listed in Table 1, parameter z_0 was varied from 10^{-5} to 10^5. For a given PSDF, the transition from the free-molecular to continuum regime was controlled by varying parameter ζ; an example of such a transition is shown in Fig. 2. Inspection of the results in Table 1 indicates that the maximum deviation between the harmonic mean, Eq. 9, and the Fuchs formula, Eq. 10, is typically within 18% and does not exceed 25% for all cases considered.

The second series of tests designed to further test the validity of Eq. 9 was performed for multimodal PSDFs. A set of 160 multimodal lognormal distributions was generated randomly, with a number of modes chosen from 2 to 4, the values of z_0 for individual modes from 10^{-4} to 10^4, the values of σ from 1.18 to 1.45, and parameter ζ from 10^{-5} to 10^2. The computed relative deviations are displayed in Fig. 3. Again, the harmonic mean approximation demonstrates a good performance, yielding relative deviations from Fuchs' formula within 27%.

The final series of tests was designed to probe Eq. 9 in dynamic modeling. Harris and Kennedy [11] numerically simulated the dynamics of an initially monodisperse soot aerosol undergoing coagulation at high pressures. They used Fuchs' formula, accounted for the van der Waals
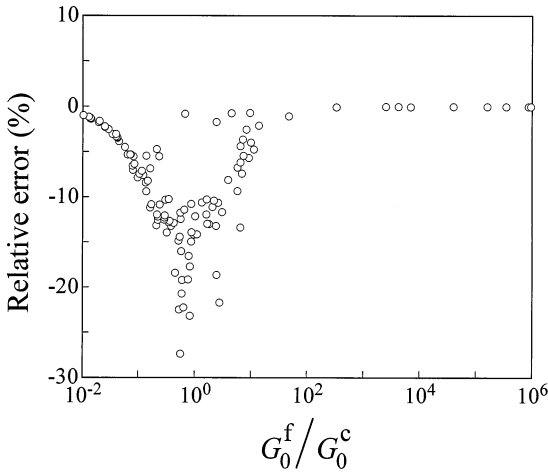
Fig. 3. Relative deviations in coagulation rate between the Fuchs formula, Eq. 10, and the harmonic-mean approximation, Eq. 9, calculated with a set of randomly generated multimodal lognormal distributions.
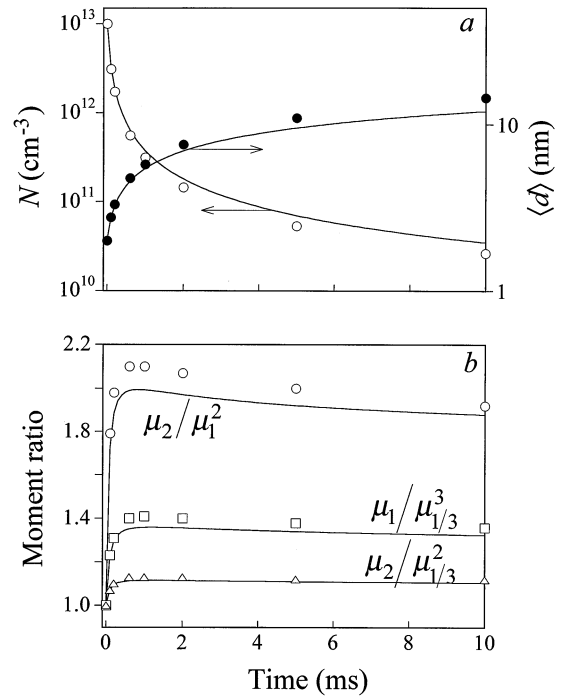

Fig. 4. Comparison between detailed simulations of Harris and Kennedy [11] (symbols) and the method of moments with Eq. 9 (lines) at pressure 20 atm, temperature 2000 K, initial particle number density 1×10^{13} cm^{-3}, and initial particle diameter 2 nm: (a) particle number density and average particle diameter; (b) moment ratios.

forces, and described the coagulating aerosol by 6500 differential equations for individual particle size bins. Our calculations were performed under the same conditions but using the method of moments with Eq. 9. The comparison between the two sets of results is shown in Fig. 4; it demonstrates that the harmonic mean approximation reproduces closely the aerosol properties. (It is worthwhile to mention that while the original computations required about two CPU hours on a CRAY X-MP, ours took less than a second on an IBM 3090/600S computer).

On the basis of these tests and considering the still remaining uncertainties in the physical model of coagulation, we conclude that Eq. 9 provides adequate accuracy. If desired, the accuracy can be improved by employing the generalized-mean-of-limits formula [23, 24],

$$G_r = [(G_r^f)^a + (G_r^c)^a]^{1/a}. \tag{11}$$

However, only a modest reduction in error could be achieved and at the expense of excessive parameterization of a in Eq. 11.

Particle Aggregation Model

Aggregation of soot particles is a well known and documented phenomenon (see [25–47] and references therein): after an initial period of "coalescent growth" soot particles begin to agglomerate. Soot agglomerates take usually the form of chain-like structures composed of nearly spherical equal-sized primary particles and are described by the well-known fractal relationship [48]

$$n = k_f \left(\frac{2R_g}{d_p} \right)^{D_f}, \tag{12}$$

where n is the number of primary particles in an aggregate, d_p is the diameter of primary particles, R_g is the radius of gyration of an aggregate, D_f is the fractal dimension, and k_f is the fractal prefactor. The main concern in most of the soot literature was to account for the fractal morphology of the aggregate cloud in optical measurements (and we employ these results for the optical part of our model; see the next section). In the present study, we are interested in modeling time evolution of soot particles, from a spherical to fractal shape, with simultaneously occurring nucleation of primary particles, coagulation of both primary and fractal particles, and deposition/oxidation of carbon mass via

reactions on soot particle surface. To our knowledge, no such modeling has been attempted, neither for soot nor other particle systems.

The mathematical formulation we present was dictated by the specific nature of our method of moments and the lack of physical models for transient behavior with coagulation and surface growth occurring simultaneously. In light of these constraints, we considered particle agglomeration at two extremes: the complete particle coalescence into perfect spheres and a fully developed regime of particle aggregation obeying Eq. 12 with constant values of D_f and k_f. In simulating a laminar premixed flame, the integration began with the coalescent limit and switched to the aggregation limit when the average particle diameter reached a critical value, $d*$. Separation in time between coalescent and non-coalescent collisions can be supported by experimental observations [49, 50] and numerical simulations [28].

The coalescent limit of coagulation was simulated by the model documented in [12]. The model for the aggregation limit was developed following similar ideas, describing the mass moments by Eqs. 1–5, but with the collision frequencies reflecting the fractal character of colliding particles [28, 51], namely,

$$\beta_{ij}^{f,a} = 2.2 \sqrt{\frac{\pi k_B T}{2 m_C} \left(\frac{1}{m_i} + \frac{1}{m_j} \right)} (d_{c,i} + d_{c,j})^2,$$
(13)

$$\beta_{ij}^{c,a} = K \left(\frac{C_i}{d_{c,i}} + \frac{C_j}{d_{c,j}} \right) (d_{c,i} + d_{c,j}).$$
(14)

Here $\beta_{ij}^{f,a}$ and $\beta_{ij}^{c,a}$ are the aggregate collision frequencies in the free-molecular and continuum regimes, respectively, and d_c is the collision diameter of a particle aggregate. Actually, the particle diameters appearing in the first set of brackets of Eq. 14 should be the mobility diameters [52, 53]. We followed Kruis et al. [54] by equating the mobility diameter to d_c, thereby assuring no discontinuity of G_c in the limit of $n \rightarrow 1$. The Cunningham slip correction factors C appearing in Eq. 14 are also evaluated on the basis of d_c.

Equation 13 is valid for $D_f \geq 2$ or for aggregates of similar sizes [28]. In the case of $D_f < 2$ and differing aggregate sizes, Eq. 13 overestimates the collision frequency because the smaller particles can pass through the larger ones without sticking. Although a scaling relationship was proposed for this regime [55], the collision frequency is not well understood in quantitative terms. Nonetheless, since the experimental values of D_f for soot aggregates are typically within a relatively narrow range just below 2, about 1.7 to 1.9 [43–45], one does not expect for Eq. 13 to introduce too large of an error [28]. Also, the aggregation limit is expected to set in close to the continuum regime of particle coagulation with the collision frequency determined primarily by Eq. 14 and not Eq. 13.

The collision diameter of an aggregate, d_c, was suggested [25, 28] to be proportional to the radius of gyration; the latter is given as

$$R_g = \frac{1}{k_f^{1/D_f}} \left(\frac{3 m_C}{4 \pi \rho} \right)^{1/3} m^{1/3} n^{1/D_f - 1/3},$$
(15)

which is obtained from Eq. 12 expressing the primary particle diameter through the total aggregate mass, m, and the number of primary particle in the aggregate, n,

$$d_p = \left(\frac{6 m_c m}{\pi \rho n} \right)^{1/3}.$$
(16)

Following Kruis et al. [54], we chose the coefficient of proportionality between d_c and R_g in such a way that in the limit of a single spherical particle, d_c becomes equal to the particle diameter, i.e.,

$$d_c = d_p n^{1/D_f} = \left(\frac{6 m_c}{\pi \rho} \right)^{1/3} m^{1/3} n^{1/D_f - 1/3}.$$
(17)

Upon substitution of Eq. 17 into Eqs. 13 and 14, and the latter into Eqs. 1, we obtain grid functions $\langle^l \varphi_{x,y} \rangle$ [10, 12, 18] that determine the $G_r^{f,a}$ terms in Eqs. 1 for the free-molecular coagulation of fractal particles,

$$\langle^l \varphi_{x,y} \rangle = 2.2 \sqrt{\frac{6 k_B T}{\rho}} \left(\frac{3 m_c}{4 \pi \rho} \right)^{1/6} \langle^l f_{x,y} \rangle,$$
(18)

where

$$\langle {}^l f_{x,y} \rangle = \frac{1}{M_0^2} \sum_{i=1}^{\infty} \sum_{j=1}^{\infty} (m_i + m_j)^l (m_i^{1/3} n_i^{1/D_f - 1/3} + m_j^{1/3} n_j^{1/D_f - 1/3})^2 m_i^{x-1/2} m_j^{y-1/2} N_i N_j,$$

$$= \sum_{k=0}^{l} \binom{l}{k} (\langle m^{x+k+1/6} n^{2/D_f - 2/3} \rangle \mu_{y+l-k-1/2} + 2\langle m^{x+k-1/6} n^{1/D_f - 1/3} \rangle \langle m^{y+l-k-1/6} n^{1/D_f - 1/3} \rangle$$

$$+ \mu_{x+k-1/2} \langle m^{y+l-k+1/6} n^{2/D_f - 2/3} \rangle).$$

Analogously, for the continuum regime, we get

$$G_0^{c,a} = K \Bigg[1 + \langle m^{1/3} n^{1/D_f - 1/3} \rangle \langle m^{-1/3} n^{1/3 - 1/D_f} \rangle + 2.514 \lambda \left(\frac{\pi \rho}{6 m_c} \right)^{1/3} (\langle m^{-1/3} n^{1/3 - 1/D_f} \rangle$$

$$+ \langle m^{1/3} n^{1/D_f - 1/3} \rangle \langle m^{-2/3} n^{2/D_f - 2/3} \rangle) \Bigg] M_0^2, \tag{19.0}$$

$$G_r^{c,a} = \frac{1}{2} K \sum_{k=1}^{r-1} \binom{r}{k} \Bigg[2\mu_k \mu_{r-k} + \langle m^{k+1/3} n^{1/D_f - 1/3} \rangle \langle m^{r-k-1/3} n^{1/3 - 1/D_f} \rangle + \langle m^{k-1/3} n^{1/3 - 1/D_f} \rangle$$

$$\cdot \langle m^{r-k+1/3} n^{1/D_f - 1/3} \rangle + 2.514 \lambda \left(\frac{\pi \rho}{6 m_c} \right)^{1/3} (\langle m^{k-1/3} n^{1/3 - 1/D_f} \rangle \mu_{r-k} + \mu_k \langle m^{r-k-1/3} n^{1/3 - 1/D_f} \rangle$$

$$+ \langle m^{k+1/3} n^{1/D_f - 1/3} \rangle \langle m^{r-k-2/3} n^{2/3 - 2/D_f} \rangle + \langle m^{k-2/3} n^{2/3 - 2/D_f} \rangle \langle m^{r-k+1/3} n^{1/D_f - 1/3} \rangle) \Bigg] M_0^2, \tag{19.r}$$

for $r = 1, 2, \ldots, 5$. The corresponding free-molecular and continuum terms, $G_r^{f,a}$ and $G_r^{c,a}$, were harmonically averaged, similar to Eq. 9.

Terms $\langle m^r n^{r'} \rangle$ appearing in Eqs. 18 and 19 are binary moments of two-dimensional particle size distribution, a function of both the aggregate mass, m, and the aggregate number of primary particles, n. Rigorous determination of the binary moments is not feasible at present, because the physical nature of such PSDF is not well understood. However, there are several ways of approximation. One of the simplest approaches is to assume

$$\langle m^r n^{r'} \rangle \approx \langle m^r \rangle \langle n^{r'} \rangle = \mu_r \pi_{r'} \tag{20}$$

where the particle mass moments μ_r are defined by Eq. 3 and those for the number of primary particles are determined by

$$\pi_r = \frac{P_r}{P_0} \tag{21}$$

and

$$P_r = \sum_{i=1}^{\infty} n_i^r N_i \tag{22}$$

Here N_i, as before, is the concentration of aggregate size class i; n_i the number of primary particles in ith aggregate; and $P_0 = M_0$ the total aggregate number density. The physical meaning of the π_r moments is as follows: $\pi_0 \equiv 1$, π_1 is the average number of primary particles in aggregates, $\pi_2 - 1$ is its variance, etc.

We tested the accuracy of approximation (20) by assuming that the primary particles are of the same size and that the mass PSDF takes a lognormal form. Both of these assumptions are well justified by experimental and modeling studies of aggregate coagulation [28, 44, 51, 56], as well as by the simulations performed during the present investigation. The results of our numerical tests showed that the maximum error

introduced by approximation (20) into the right-hand side of Eqs. 1 is no larger than 20%, and typically smaller than that. Hence, Eq. 20 was adopted for the present study.

Moments P_r were determined by solving the equations

$$\frac{dP_1}{dt} = R_0 \tag{23.1}$$

$$\frac{dP_r}{dt} = R_0 + H_r, \quad r = 2, \cdots, \tag{23.r}$$

simultaneously with Eqs. 1; here R_0 is the rate of particle inception and H_r is the contribution from aggregate coagulation,

$$H_r = \frac{1}{2} \sum_{k=1}^{r-1} \binom{r}{k} \left(\sum_{i=1}^{\infty} \sum_{j=1}^{\infty} n_i^k n_j^{r-k} \beta_{ij}^a N_i N_j \right), \tag{24}$$

and β_{ij}^a the collision frequency of aggregates. The summations in Eq. 24 were dealt with similarly to the G_r terms of Eqs. 1 [10, 12, 18]. Thus, for the free-molecular regime, we define

$$H_r^f = \frac{1}{2} \langle \psi_r \rangle \tag{25}$$

with $\langle \psi_r \rangle$ evaluated by interpolation between grid functions

$$\langle^l\psi_r \rangle = 2.2 \sqrt{\frac{6k_B T}{\rho}} \left(\frac{3m_c}{4\pi\rho} \right)^{1/6} \langle^l h_r \rangle, \tag{26}$$

where

$$\langle^l h_r \rangle = \sum_{k=0}^{l} \binom{l}{k} \sum_{q=1}^{r-1} \binom{r}{q} (\langle m^{k+1/6} n^{q+2/D_f-2/3} \rangle \langle m^{l-k-1/2} n^{r-q} \rangle + 2\langle m^{k-1/6} n^{q+1/D_f-1/3} \rangle$$

$$\cdot \langle m^{l-k-1/6} n^{r-q+1/D_f-1/3} \rangle + \langle m^{k-1/2} n^q \rangle \langle m^{l-k+1/6} n^{r-q+2/D_f-2/3} \rangle).$$

Similarly, for the continuum regime of agglomeration, we have

$$H_r^c = \frac{1}{2} K \sum_{k=1}^{r-1} \binom{r}{k} \left[2\pi_k \pi_{r-k} + \langle m^{1/3} n^{k+1/D_f-1/3} \rangle \langle m^{-1/3} n^{r-k+1/3-1/D_f} \rangle + \langle m^{-1/3} n^{k+1/3-1/D_f} \rangle \right.$$

$$\cdot \langle m^{1/3} n^{r-k+1/D_f-1/3} \rangle + 2.514\lambda \left(\frac{\pi\rho}{6m_c} \right)^{1/3} (\langle m^{-1/3} n^{k+1/3-1/D_f} \rangle \pi_{r-k} + \pi_k \langle m^{-1/3} n^{r-k+1/3-1/D_f} \rangle$$

$$+ \langle m^{1/3} n^{k+1/D_f-1/3} \rangle \langle m^{-2/3} n^{r-k+2/3-2/D_f} \rangle + \langle m^{-2/3} n^{k+2/3-2/D_f} \rangle \langle m^{1/3} n^{r-k+1/D_f-1/3} \rangle) \left] M_0^2. \right.$$

$$\tag{27}$$

The binary moments appearing in these equations were resolved via approximation (20) and the fractional-order moments were obtained by interpolation between the whole-order moments using the approach described by Frenklach and Harris [10]. Because the primary particles have reportedly a narrow distribution [44, 56], a two-moment model (i.e., with differential equations 23 for P_1 and P_2) was assumed to provide sufficient accuracy. The corresponding free-molecular and continuum terms, H_r^f and H_r^c, were harmonically averaged, similar to Eq. 9.

Particle aggregation also affects the surface growth terms, W_r in Eqs. 1, because the aggregate surface area is larger than that of a spherical particle with the same mass. We expressed the surface area of an aggregate as

$$S^a = \pi d_p^2 n = \pi \left(\frac{6m_c}{\pi\rho} \right)^{2/3} m^{2/3} n^{1/3}, \tag{28}$$

which is obtained by assuming that the entire outer surface area of an aggregate is accessible for surface reactions; in other words, we assumed that the primary particles have point contacts and neglected "necking." A theoretical analysis of Rosner and Tandon [57] shows that under the conditions examined in the present

study the reduction in accessible aggregate surface area due to diffusion limitations should be negligible [58]. Substituting Eq. 28 into Eq. 4 and performing the summations, we obtain

$$W_r^a = k_s C_g \alpha \chi_s \pi \left(\frac{6m_c}{\pi\rho} \right)^{2/3} \sum_{k=0}^{r-1} \binom{r}{k} \Delta^{r-k} \langle m^{k+2/3} n^{1/3} \rangle \tag{29}$$

with the binary moments evaluated using Eq. 20, as described earlier. The same chemical reaction mechanism [3] was assumed for both aggregated and nonaggregated particles.

Optical Properties of Particle Ensemble

A common approach for characterization of soot formation in flame environments is a combined laser-scattering and extinction method [59, 60]. Physical properties of soot particle aerosol, such as soot volume fraction, particle number density, and average particle size, are often derived from measuring volumetric scattering cross section, Q_{vv}, and extinction coefficient, k_{ext}. These properties were computed in the present study employing two optical models, one for the complete coalescence and the other for the aggregation regime. During the coalescence regime, Q_{vv} and k_{ext} were obtained from the computed moments using the formalism [2, 12] based on the Penndorf expansion [61] of the Mie equations [62, 63]. The optical model used for the aggregation regime is described below.

Optical properties of soot aggregates were described using the fractal aggregate theory founded on the Rayleigh-Debye-Gans approximation. Within this approximation, the volumetric scattering cross section and the extinction coefficient are given by [36]

$$k_{ext} = \left[\frac{\pi^2}{\lambda_{ext}} E(\tilde{m}) \langle n d_p^3 \rangle + \frac{2\pi}{3} \left(\frac{\pi}{\lambda_{ext}} \right)^4 F(\tilde{m}) \right.$$
$$\left. \cdot \langle n^2 d_p^6 g(2\pi R_g/\lambda_{ext}) \rangle \right] M_0, \tag{30}$$

$$Q_{vv} = \frac{1}{4} \left(\frac{\pi}{\lambda_{sca}} \right)^4 F(\tilde{m}) \langle n^2 d_p^6 S(qR_g) \rangle M_0, \tag{31}$$

where λ_{sca} and λ_{ext} are the scattering and extinction radiation wavelengths, respectively; $q = 4\pi \sin(\theta/2)/\lambda_{sca}$ is the modulus of scattering

vector; θ is the scattering angle (equal to 90° in the experimental measurements of Jander and co-workers [64]); and $E(\tilde{m})$ and $F(\tilde{m})$ are functions of soot complex refractive index, $\tilde{m}$,

$$E(\tilde{m}) = -\text{Im} \left(\frac{\tilde{m}^2 - 1}{\tilde{m}^2 + 2} \right),$$

$$F(\tilde{m}) = \left| \frac{\tilde{m}^2 - 1}{\tilde{m}^2 + 2} \right|^2.$$

The aggregate shape factor $S(qR_g)$ appearing in Eq. 31 was adopted in the form suggested by Dobbins and Megaridis [36],

$$S(qR_g) = \begin{cases} \exp\left(-\frac{(qR_g)^2}{3} \right) & (32.1) \\ \left(\frac{3D_f}{2e(qR_g)^2} \right)^{D_f/2} & (32.2) \end{cases}$$

for the Guinier and power-law regimes, respectively, with the crossover between the two at $(qR_g)^2 = 3D_f/2$; here e is the base of the natural logarithm. Evaluation of the aggregate total scattering factor g appearing in Eq. 30 followed the works of Dobbins and Megaridis [36] and Köylü and Faeth [42] but in a rederived form, as explained in the Appendix.

Substitution of Eq. 16 into Eqs. 30 and 31 results in

$$k_{ext} = \left(\left(\frac{6\pi m_c}{\lambda_{ext}\rho} E(\tilde{m}) \langle m \rangle + \frac{6}{\pi} \left(\frac{2\pi^2 m_c}{\lambda_{ext}^2 \rho} \right)^2 F(\tilde{m}) \right. \right.$$
$$\left. \left. \cdot \langle m^2 g(2\pi R_g/\lambda_{ext}) \rangle \right) M_0 \right. \tag{33}$$

$$Q_{vv} = 9F(\tilde{m}) \left(\frac{\pi m_c}{\lambda_{sca}^2 \rho} \right)^2 \langle m^2 S(qR_g) \rangle M_0 \tag{34}$$

where R_g is expressed as a function of m and n via Eq. 15. Owing to the rapidly increasing size of particles in the aggregation limit, the moments appearing in Eqs. 33 and 34 cannot be evaluated using the Penndorf expansion [61]. Indeed, the Penndorf series expansion converges only at $\text{Re}\{\tilde{m}\} \pi d/\lambda_{rad} \leq 1$, where $\text{Re}\{\tilde{m}\}$ is the real part of the complex refractive index $\tilde{m}$, d is the particle diameter, and λ_{rad} is the radiation wavelength. For $\tilde{m} = 1.57 - 0.56i$ at $\lambda_{rad} = 488$ nm [65], the convergence criterion is satisfied for particle diameters below about 100 nm; this is fulfilled during the initial

stages of soot particle inception but limits applicability of this approach for simulation of particle aggregation.

Taking into consideration that in the aggregation regime particle distribution approaches an asymptotic, self-preserving distribution rather quickly [25, 44, 51], the PSDF moments for the calculation of optical properties were obtained by direct integration using a prescribed functional form of PSDF. For the mass moments, we adopted a bimodal lognormal distribution function,

$$\frac{1}{3m\sqrt{2\pi}}\left[\frac{a}{\ln\sigma_1}\exp\left(-\frac{\ln^2(m/m_{g,1})}{18\ln^2\sigma_1}\right)\right.$$

$$\left.+\frac{1-a}{\ln\sigma_2}\exp\left(-\frac{\ln^2(m/m_{g,2})}{18\ln^2\sigma_2}\right)\right], \quad (35)$$

reported to provide a realistic description of soot aerosols in flame environments [33, 66]. Parameters $m_{g,1}$, σ_1, $m_{g,2}$, σ_2, and a were obtained by fitting the computed moments M_r (all five computed PSDF moments could be fitted to better than 1% accuracy for the aggregation regime, but larger errors, up to 180%, were obtained for the coalescent coagulation). Analogously, the distribution function for the aggregate number of primary particles was represented with a single-mode lognormal distribution function,

$$\frac{1}{n\sqrt{2\pi}\ln\sigma_3}\exp\left(-\frac{\ln^2(n/n_g)}{2\ln^2\sigma_3}\right), \quad (36)$$

with $n_g = \pi_1^2/\sqrt{\pi_2}$ and $\ln\sigma_3 = \sqrt{\pi_2}/\pi_1$. The optical properties were then obtained by numerical integration over distributions (35) and (36). Standard techniques described by Bohren and Huffman [63] were used for the Mie calculations.

We must emphasize that explicit analytical expressions (35) and (36) were used only for the calculation of soot optical properties of particle aggregates. The PSDF moments employed in the dynamic simulation of soot aerosol were determined by the technique of interpolation described earlier in this section, i.e., without prescribing any functional form to PSDF.

COMPUTATIONAL DETAILS

The chemical part of the model, i.e., the gas-phase reactions and surface growth/oxidation mechanism, were the same as described in Kazakov et al. [3] and references therein. As before, the gas-phase composition was obtained using the Sandia burner code [67] and the computed profiles of H, OH, H_2, H_2O, O_2, and C_2H_2 together with the rate of pyrene formation were used for simulation of polycyclic aromatic hydrocarbon (PAH) growth beyond pyrene and soot formation with an in-house code [12]. The PAH growth was described using the technique of linear lumping [12, 68].

The gas mean free path, λ, of the Knudsen number was computed for the bath gas N_2, and the gas viscosity η of the constant K, first appearing in Eq. 7, was calculated with the formula of Sutherland [69], $\eta = 1.458 \times 10^{-5} T^{3/2}/(T + 110.4)$ g cm^{-1} s^{-1}, found for the conditions of the present study to be within 4.5% of the Wilke semiempirical formula [70] implemented in the Sandia multicomponent transport package [71]. The optical properties of soot were calculated using $\bar{m} = 1.57 - 0.56i$ [65] for $\lambda_{sca} = 488$ and $\lambda_{ext} = 633$ nm, the same as in the experimental study of simulated flames.

Soot formation was numerically simulated for the flames considered in our previous study [3]. Since the phenomena investigated in the present study are expected to come forth at higher pressures and higher carbon densities, we focused primarily on two 10 bar C_2H_4-air flames with the highest C/O ratios, Flame 1 (C/O = 0.68, cold gas velocity 6 cm/s) and Flame 2 (C/O = 0.67, cold gas velocity 3 cm/s) of [3]. The experimental observations of these flames gave an appearance of a catastrophic decrease in coagulation rates that could not be rationalized within the classical theory of Brownian coagulation [15, 64]. The present numerical simulations exhibited similar trends for both flames; however, the investigated phenomena were more pronounced for Flame 2 because of its higher soot volume fraction and longer reaction time as compared to Flame 1. Therefore, numerical results obtained for Flame 2 are reported in greater detail.

RESULTS AND DISCUSSION

Effect of More Complete Description of Particle Coagulation

We started by examining sensitivity of model predictions for soot particle properties to the more complete formulation of particle coagulation described in the previous section. Two computer runs were carried out for each flame. In the first run, similar to our previous study [3], the free-molecular regime of coagulation was assumed for the entire duration of the process. In the second run, particle coagulation was described by Eq. 9, i.e., with the transition and continuum regimes taken into account. The results obtained for Flame 2 are depicted in Fig. 5. As can be seen, the predicted soot volume fraction, particle number density, and surface area are all significantly increased with the more complete treatment of coagulation. This is caused by lower coagulation rates in the transition and continuum regimes as compared to the free-molecular one (cf. Fig. 1). It is pertinent to mention that a similar test with a 1 bar ethylene-air flame, Flame 4 in [3] (C/O = 0.69, cold gas velocity 5.9 cm/s), produced no measurable effect.

Transition from one regime of coagulation to another, with the increase in soot particle size, affects not only physical properties of soot aerosol, such as those shown in Fig. 5a–c but also the shape of the distribution function itself. Figure 5d displays the computed dispersion, a measure of the distribution width. It is apparent that inclusion of the transition and continuum regimes of coagulation results in a narrower PSDF (i.e., in a lower dispersion) and a much faster approach to the self-preserving distribution (i.e., to the asymptotic value of dispersion of about 2) as compared to the case of free-molecular coagulation. Such trend is expected. As larger particles enter the transition regime, their coagulation rate decreases; the smaller particles, on the other hand, remain in the free-molecular regime. As a result, the fraction of small particles in the soot particle cloud is decreased and PSDF is narrowed. A similar effect was reported by Harris and Kennedy [11] from their detailed solution of master equations
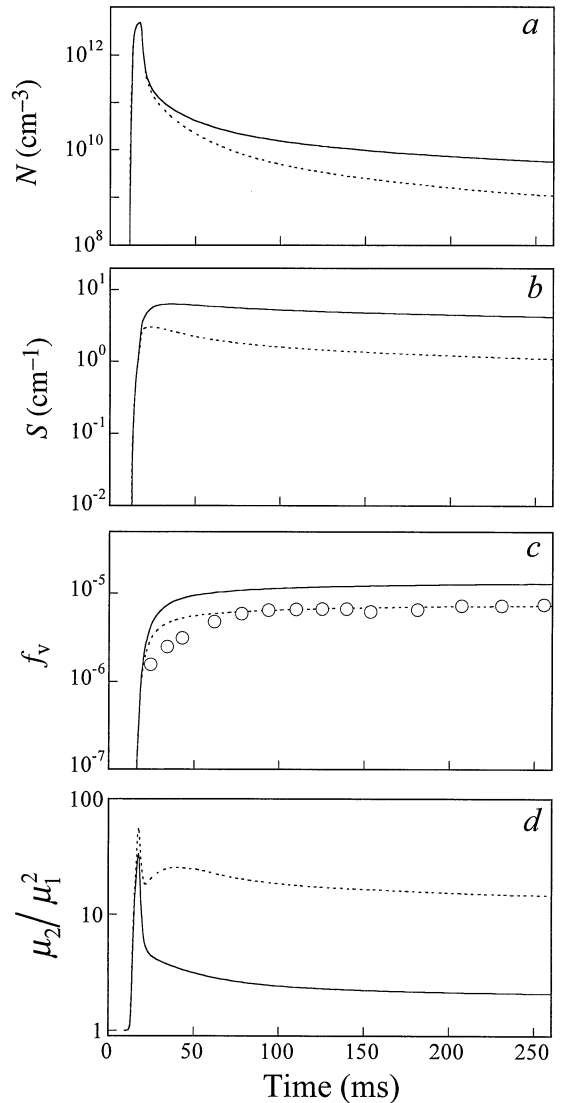

Fig. 5. Effect of different coagulation regimes on calculated soot particle properties for Flame 2: **(a)** number density; **(b)** surface area; **(c)** volume fraction; **(d)** dispersion of size distribution. Dotted lines are calculated assuming the free-molecular regime of coagulation during the entire process; solid lines are calculated with transition and continuum regimes included. (Aggregation is not included). The symbols in c represent experimental measurements for Flame 2 [3, 64].

for coagulation of an initially monodispersed aerosol at 20 and 50 atm (Fig. 4b).

To accommodate the changes made in the model, we refitted parameter α of Eq. 4 to match k_{ext}: it was lowered from 0.43 to 0.33 for
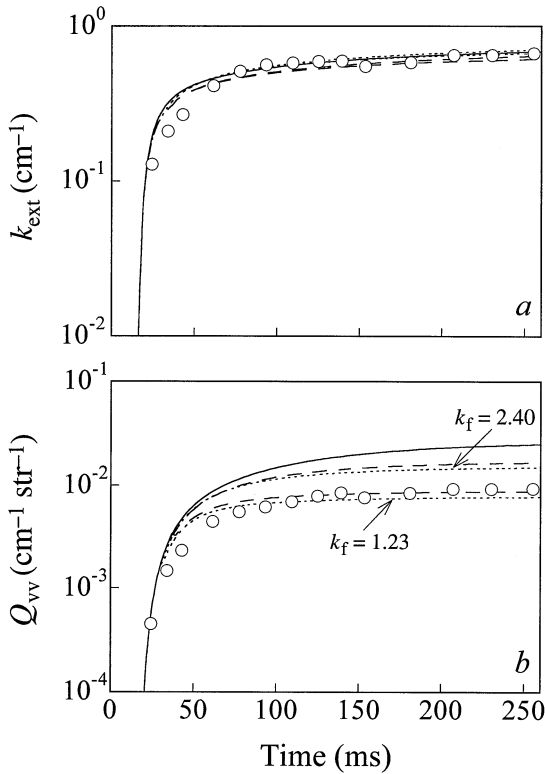
Fig. 6. Comparison of model predictions and experimental data for soot optical properties of Flame 2: **(a)** extinction coefficient; **(b)** volumetric scattering cross section. Solid lines are computed with all regimes of coagulation but no aggregation included and using the Mie theory for optical properties; dotted and dashed lines are computed with the fractal aggregation model using d^* equal to 25 and 30 nm, respectively; symbols are the experimental data [64].
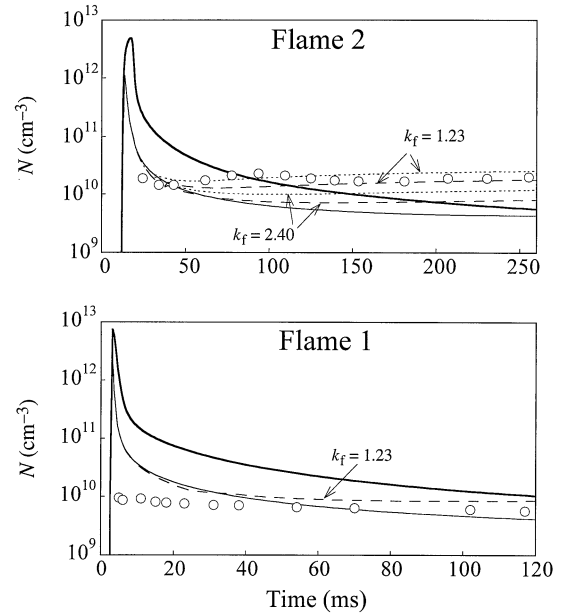

Fig. 7. Comparison of model predictions and experimental data for soot particle number density in Flames 1 and 2. Thick solid lines represent the *actual* number density predicted by the numerical model; thin solid lines represent *apparent* number density obtained from k_{ext} and Q_{vv} simulated using the complete-coalescence model and Mie theory; dotted and dashed lines represent *apparent* number densities obtained from k_{ext} and Q_{vv} simulated using the fractal aggregation model with d^* equal 25 and 30 nm, respectively; symbols represent experimental data [64]. The data for Flame 2 were obtained by interpolation between two similar flames with C/O equal to 0.672 and 0.696 [64].

Flame 2 and from 0.33 to 0.29 for Flame 1, as compared to our previous study of the same flames [3]. The quality of fit, for both k_{ext} that was fitted and Q_{vv} that was not, is demonstrated in Fig. 6. We note, however, that the readjustments of α were done solely for the purpose of the particle coagulation analysis of these specific flames. Reevaluation of the global dependence of α on temperature [3] should include new developments in inception [72] and surface [73] reaction kinetics, which is beyond the scope of the present study.

To investigate the long-time behavior of particle number density, N, that led to the puzzling observations of Feldermann et al. [15], we compared the values of N predicted by our numerical model, referred to as *actual* particle number densities, to those obtained from the predicted

by our model values of k_{ext} and Q_{vv} through deconvolution with the Mie theory and assumption of monodispersed PSDF, i.e., in exactly the same way as was done in the original experimental study [14, 64]. Determined in this manner, the particle number densities will be referred to as *apparent* and denoted by N_{app}. The corresponding actual, apparent, and experimental particle number densities for Flames 1 and 2 are displayed in Fig. 7. As can be seen, the actual and apparent particle number densities are reasonably close to each other and to the experimental data points. Nonetheless, the model fails to predict correctly the observed time evolution of N in the post-flame zone: while the experiment shows a nearly time independent profile, the model predicts a monotonically decreasing function of time. Thus, while the inclusion of the transition and continuum

regimes of coagulation does improve the agreement of the model with experiment, this correction alone is not sufficient to fully account for the observations of Feldermann et al. [15].

Effect of Soot Particle Aggregation

As before, we tested the additional part of the model, now describing particle aggregation, in a series of sensitivity runs. The present particle aggregation model was developed assuming a constant aggregate fractal dimension; we used $D_f = 1.8$, typical of soot aggregates observed in flame environments [43–45].

One of the introduced assumptions is a switch from complete coalescence to aggregation when the computed average particle diameter, $\langle d_p \rangle$, reaches a critical value, d^*. Numerical simulations indicated that after the switch to the regime of aggregation, the value of $\langle d_p \rangle$ does not increase appreciably (Fig. 8a). We therefore assumed, having no other information, that d^* can be approximated by an experimental value of primary particle diameter.

The size of primary particles has not been reported for the flames examined in the present study; however, for a similar, 15 bar flame, primary soot particles of 30 nm diameter have been observed by transmission electron microscopy [74]. Based on this, we performed numerical simulations with d^* equal 25 and 30 nm. Figure 8 compares the results of these runs for Flame 2 along with those obtained without aggregation included. The simulations demonstrate a strong effect of aggregation on the time evolution of primary particle size (Fig. 8a). In the absence of aggregation, the particle size increases continuously due to coalescence; after the aggregation is switched on, the average primary particle diameter increases only slightly, due to surface growth, and remains nearly constant once the surface growth rate decreases.

With the onset of aggregation, as expected, the aggregate number of primary particles starts to increase from its complete-coalescence value of unity (Fig. 8b). The results shown in Fig. 8b demonstrate that delaying the onset of aggregation, i.e. using a larger d^*, reduces the average number of primary particles per aggregate.
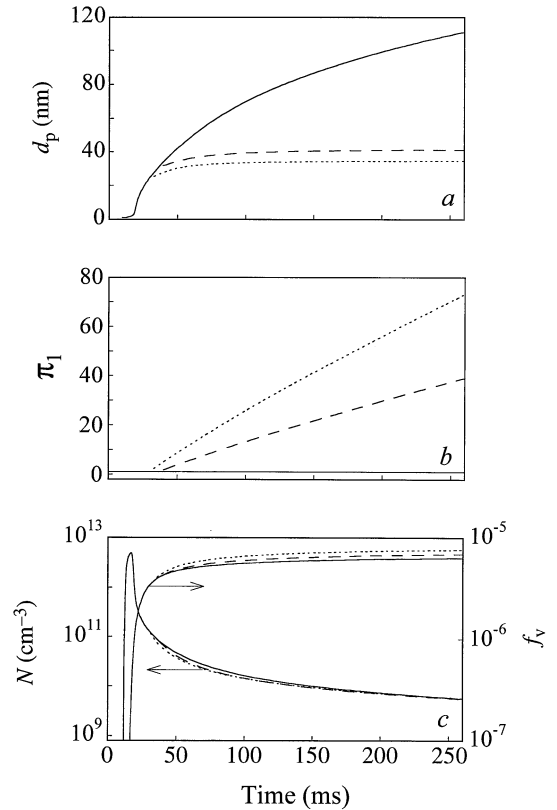
The aggregation has only a weak effect on the

Fig. 8. Effect of particle aggregation on calculated soot properties for Flame 2: **(a)** average primary particle diameter, **(b)** average number of primary particles per aggregate, **(c)** aggregate number density and soot volume fraction. Solid lines are computed with the complete-coalescence model; dotted and dashed lines are computed with particle aggregation included and d^* equal to 25 and 30 nm, respectively.

predicted soot volume fraction for the flames considered (Fig. 8c): the difference between the complete-coalescence and aggregation cases does not exceed 14%. The reason for this is as follows. When the aggregate surface area begins to deviate substantially from that of the mass-equivalent sphere, the surface growth rate happens to vanish. Also shown in Fig. 8c is that the particle number densities, computed for complete coalescence and aggregation, are nearly identical to each other. At high pressures, coagulation enters quickly the continuum regime with the rate, given by Eq. 14, only weakly dependent on D_f [51].

Evaluation of aggregate optical properties via Eqs. 30 and 31 requires an explicit knowledge of the fractal prefactor, k_f in Eq. 12. Literature

recommendations for k_f of soot aggregates varies from about 1.0 to 3.0 [32, 43, 45–47, 75]. We performed calculations using two recently published values, 1.23 [32] and 2.4 [43]. A comparison of the optical properties computed for Flame 2 is depicted in Fig. 6. As can be seen, the calculated profiles of the extinction coefficient are very close to each other, thus showing little sensitivity to k_f and d^*, or to the particle aggregation in general. On the other hand, the scattering efficiency is shown to significantly deviate when aggregation is included, with a nearly linear dependence on the fractal prefactor. At the same time, the dependence of Q_vv on d^* is relatively weak: increasing d^* results in a larger size yet a smaller number of primary particles, and these two factors evidently compensate each other. We note that while a better fit in Figs. 6b and 7b is obtained using the lower k_f value, it is the higher one which is recommended by recent evaluations [43–45]; however, one cannot favor the lower k_f value based solely on the present results because the factor-of-2 difference is of the same magnitude as other uncertainties of the model.

Finally, we performed the same numerical test as in the preceding section: the computed values of Q_vv and k_ext were deconvoluted using the Mie theory and monodisperse PSDF assumption to produce the apparent particle number densities. The results, depicted in Fig. 7, indicate that the inclusion of particle aggregation in flame simulations improves the agreement of the model with experiment, now predicting correctly that while the *actual* number density decreases monotonically the *apparent* number density of soot particles is leveling off or even slightly increasing with the flame height. In other words, the observations of Feldermann et al. [15] can be explained by differing optical cross sections due to particle aggregation.

Our conclusion is in accord with soot measurements of Dobbins et al. [35] and Puri et al. [46] in atmospheric ethylene laminar diffusion flames, who showed that data reduction with a fractal-aggregate theory predicts a monotonic decrease in the aggregate number density whereas the Mie theory yields almost a constant particle number density along the flame streamline.

This effect can be qualitatively explained using a simplified analytical analysis using the
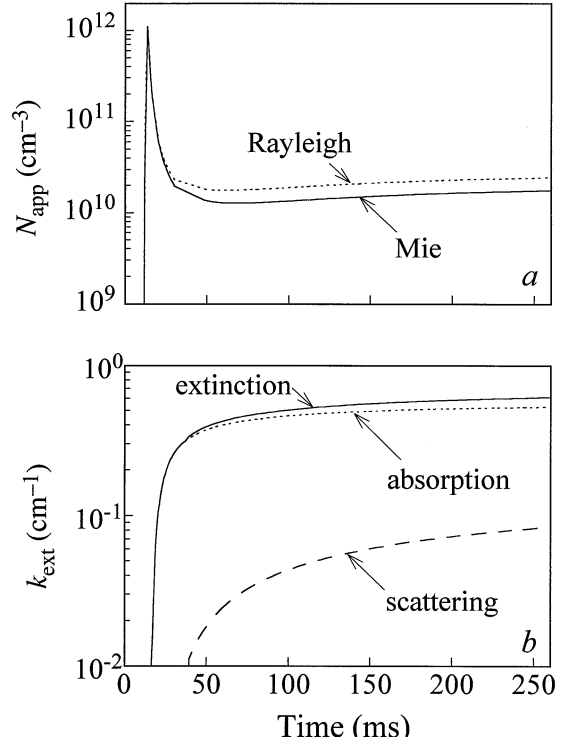

Fig. 9. **(a)** Apparent soot particle number density deconvoluted from the optical properties computed with the fractal aggregate theory for Flame 2; **(b)** Comparison of absorption, scattering, and extinction coefficients computed with the fractal aggregate theory for Flame 2. The aggregate theory computations were performed using $d^* = 30$ nm and $k_\mathrm{f} = 1.23$.

Rayleigh approximation of the Mie theory [62, 63]. Within this approximation, we have [60, 76]

$$k_\mathrm{ext} = \frac{\lambda_\mathrm{ext}^2}{\pi} E(\tilde{m}) \left(\frac{\pi d_\mathrm{app}}{\lambda_\mathrm{ext}} \right)^3 N_\mathrm{app}, \qquad (37)$$

$$Q_\mathrm{vv} = \frac{\lambda_\mathrm{sca}^2}{4\pi^2} F(\tilde{m}) \left(\frac{\pi d_\mathrm{app}}{\lambda_\mathrm{sca}} \right)^6 N_\mathrm{app}. \qquad (38)$$

From Eqs. 37 and 38, the apparent particle number density can be expressed as

$$N_\mathrm{app} = \frac{\lambda_\mathrm{ext}^2}{4\lambda_\mathrm{sca}^4} \frac{F(\tilde{m})}{E^2(\tilde{m})} \frac{k_\mathrm{ext}^2}{Q_\mathrm{vv}} \propto \frac{k_\mathrm{ext}^2}{Q_\mathrm{vv}} \qquad (39)$$

whose numerical predictions do not fall too far from the Mie solution (Fig. 9a). If the particles are actually aggregated, their optical properties obey the relationships

$$k_\mathrm{ext} \propto N n d_\mathrm{p}^3, \qquad (40)$$

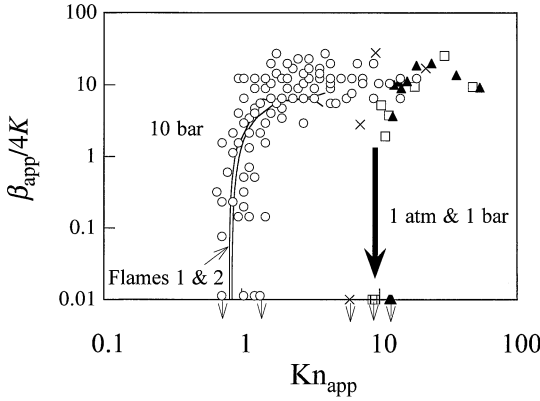$$Q_\mathrm{vv} \propto N n d_\mathrm{p}^{6-D_\mathrm{f}}. \qquad (41)$$

Fig. 10. Apparent soot particle collision frequency derived from optical measurements: ○ a set of 10 bar C_2H_4-air laminar premixed flames [15]; × atmospheric C_2H_4 laminar diffusion flame [46], □ atmospheric C_3H_8-O_2 laminar premixed flame [50]; ▲ 1 bar C_2H_4-O_2 laminar premixed flame [77]; lines are predictions of the present fractal aggregate model, computed with $d^* = 30$ nm and $k_f = 1.23$.

Relationship 40 is obtained by neglecting scattering, the second term in Eq. 33, whose contribution is indeed rather small for the conditions tested (Fig. 9b). Expression 41 is based on the assumption that soot aggregates are large enough to satisfy the criterion for the power-law regime, Eq. 32.2. Substitution of (40) and (41) into (39) results in

$$N_{app} \propto Nn d_p^{D_f}. \tag{42}$$

In the regime of cluster-cluster aggregation (as, e.g., in the post-flame zone of a laminar premixed flame or around the soot peak in a laminar diffusion flame), the following assumptions can be made: fractal dimension $D_f \approx$ const [48]; primary particle diameter $d_p \approx$ const, as the surface growth rate decays; and the total number density of primary particles in the system $Nn \approx$ const, as nucleation becomes negligible. Then, according to Eq. 42, the apparent particle number density N_{app} must be also constant.

Looking at the same phenomenon in the manner used by Feldermann et al. [15], we display in Fig. 10 experimental and modeling results as apparent collision frequency,

$$\beta_{app} = -\frac{2}{N_{app}^2} \frac{dN_{app}}{dt} \tag{43}$$

with dN_{app}/dt determined by numerical differentiation of N_{app} profiles, vs apparent Knudsen number, $Kn_{app} = 2\lambda/d_{app}$. Although numerical differentiation is associated with a large scatter, the data exhibit a clear trend: for a given pressure, the apparent coagulation rate approaches zero at similar values of the apparent Knudsen number. Furthermore, the difference in the limiting Kn_{app} values between the 10 and 1 bar flames is primarily due to the change in the mean free path and at both pressures the limit appears to be reached at essentially the same apparent soot particle size d_{app}, about 60 to 100 nm. The present detailed aggregation model reproduces this effect (and the experimental data themselves) correctly (Fig. 10), and the simplified analysis is able to explain it. Indeed, from Eqs. 37 and 38, we can express the apparent particle diameter as

$$d_{app} = \left(\frac{4}{\pi^2} \frac{\lambda_{sca}^4}{\lambda_{ext}} \frac{E(\tilde{m})}{F(\tilde{m})} \frac{Q_{vv}}{k_{ext}} \right)^{1/3}. \tag{44}$$

Substitution of (40) and (41) into (44) gives

$$d_{app} \approx (k_f d_p^{3-D_f})^{1/3} \left(\frac{3 D_f \lambda_{sca}^2}{4\pi^2 e} \right)^{D_f/6}. \tag{45}$$

Given that flame measurements of k_f, D_f, and d_p result in relatively narrow ranges for all of these parameters [43–45], Eq. 45 predicts d_{app} to be nearly a constant as well.

CONCLUSIONS

Consideration of the transition and continuum coagulation and the fractal-aggregate formation appears to produce significant effects on modeling soot formation in laminar premixed flames at elevated pressures. Among the findings is an explanation of the unusual behavior reported by Feldermann et al. [15], who observed that in the post-flame zone of high-pressure laminar premixed flames soot particle number density remains nearly constant, whereas the classical theory of Brownian coagulation predicts its monotonic decrease.

More generally, the present work demonstrates that the method of moments can be extended preserving the numerical efficiency and the physical rigor of the prior formalism [10], by inclusion of just two additional moment equations and without prescribing a mathematical form to the

particle size distribution function, to provide a quantitative description for fractal growth of soot aerosol. Assumptions made, like the empirical choice of the switch-off particle diameter d^* and the use of Eq. 20, can be removed when the physics of simultaneous particle aggregation and surface growth is understood in quantitative terms.

APPENDIX: AGGREGATE TOTAL SCATTERING FACTOR

Within the Rayleigh-Debye-Gans approximation, the aggregate total scattering factor $g(x)$ appearing in Eq. 30 is related to the shape factor $S(qR_g)$ through the following equation [36, 42],

$$g(x) = \frac{3}{8} \int_0^\pi S(2x \sin (\theta/2))(1$$

$$+ \cos^2 \theta) \sin \theta \, d\theta, \tag{A1}$$

where $x = 2\pi R_g/\lambda_{\text{ext}}$. In their original formulation, Dobbins and Megaridis [36] considered the limiting behavior of $g(x)$ and derived an interpolation equation between the two limits.

Köylü and Faeth [42] suggested to analytically integrate Eq. A1. The integration must be per-

formed for two cases. In the first case, for $x \leq (3D_f/8)^{1/2}$, the light scattering occurs only in the Guinier regime for $0 \leq \theta \leq \pi$, and $g(x)$ is given by

$$g_a(x) = \frac{3}{8} \int_0^\pi \exp \left(-\frac{(2x \sin \theta/2)^2}{3} \right)(1$$

$$+ \cos^2 \theta) \sin \theta \, d\theta. \tag{A2}$$

In the second case, for $x > (3D_f/8)^{1/2}$, the switch from the Guinier to the power-law regime occurs at $0 \leq \theta \leq \pi$, and the integration domain should be divided into two regions,

$$g_b(x) = I_1(x) + I_2(x), \tag{A3}$$

where I_1 is the contribution from the Guinier regime,

$$I_1(x) = \frac{3}{8} \int_0^{\theta_0} \exp \left(-\frac{(2x \sin \theta/2)^2}{3} \right)(1$$

$$+ \cos^2 \theta) \sin \theta \, d\theta, \tag{A4}$$

I_2 the contribution from the power-law regime,

$$I_2(x) = \frac{3}{8} \int_{\theta_0}^\pi \left(\frac{8ex^2 \sin^2 \theta/2}{3D_f} \right)^{-D_f/2}(1$$

$$+ \cos^2 \theta) \sin \theta \, d\theta, \tag{A5}$$

and $\theta_0 = 2 \arcsin [(3D_f/8x^2)^{1/2}]$ the angle at which the switch between the two regimes occurs. Equations A3–A5 are exact. In their integration, Köylü and Faeth [42] introduced approximations.

In the present study, the exact analytical integrals of Eqs. A3–A5 were found [78] without making approximations,

$$g_a(x) = \frac{9}{32x^6} [4x^4 - 6x^2 + 9 - (4x^4 + 6x^2$$

$$+ 9)e^{-4x^2/3}] \tag{A6}$$

and

$$g_b(x) = \frac{9}{32x^6} \left[4x^4 - 6x^2 + 9 - \left(4x^4 - 3(2 + D_f)x^2 + 9 + \frac{9}{2} D_f + \frac{9}{8} D_f^2 \right)e^{-D_f/2} \right]$$

$$- \frac{3e^{-D_f/2}}{(D_f - 2)(D_f - 4)(D_f - 6)} \left\{ \left(\frac{3D_f}{8x^2} \right)^{D_f/2} (D_f^2 - 6D_f + 16) - \frac{9D_f}{32x^6} \left[\left(\frac{4}{3} D_f^2 - \frac{40}{3} D_f \right. \right. \right.$$

$$\left. \left. \left. + 32 \right)x^4 - (D_f^3 - 8D_f^2 + 12D_f)x^2 + \frac{3}{8} D_f^4 - \frac{9}{4} D_f^3 + 3D_f^2 \right] \right\}. \tag{A7}$$
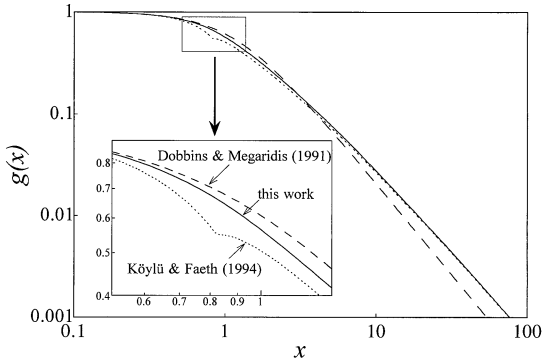
Fig. A1. Comparison of the aggregate total scattering factor computed with the expressions of Dobbins and Megaridis [36], Köylü and Faeth [42], and Eqs. A6–A8 of the present study with $D_f = 1.8$.

Equations A6 and A7 are displayed in Fig. A1, together with the $g(x)$ functions of Dobbins and Megaridis [36] and Köylü and Faeth [42]. All three expressions exhibit the same behavior at small x. At large x, Dobbins and Megaridis's result [36] deviates from Eq. A7; the reason for this is an inexact coefficient of proportionality adopted by these authors for the large-x limit. Equations derived by Köylü and Faeth [42] yield the correct asymptotic behavior for both small- and large-x limits. However, they deviate from the exact solution with a discontinuity in the first derivative at $x = (3D_f/8)^{1/2}$. This problem originates from approximations made to the aggregate shape function $S(qR_g)$.

We note that direct evaluation of Eq. A6 causes large numerical roundoff errors when x approaches zero. To avoid this problem, we used the Taylor series expansion of Eq. A6,

$$g(x) = 1 - \frac{2}{3}x^2 + \frac{14}{45}x^4 - \frac{44}{405}x^6 + \frac{256}{8505}x^8, \quad \text{(A8)}$$

for the computation of $g(x)$ at $x < 0.1$. In Eq. A8, the first two right-hand-side terms are the same as those of Köylü and Faeth [42].

REFERENCES

1. Frenklach, M., and Wang, H., *Twenty-Third Symposium (International) on Combustion*, The Combustion Institute, Pittsburgh, 1991, pp. 1559–1566.
2. Markatou, P., Wang, H., and Frenklach, M., *Combust. Flame* 93:467–482 (1993).
3. Kazakov, A., Wang, H., and Frenklach, M., *Combust. Flame* 100:111–120 (1995).
4. Colket, M. B., and Hall, R. J., in *Soot Formation in Combustion: Mechanisms and Models* (H. Bockhorn, Ed.), Springer-Verlag, Berlin, 1994, pp. 442–468.
5. Mauss, F., Schäfer, T., and Bockhorn, H., *Combust. Flame* 99:697–705 (1994).
6. Mauss, F., and Bockhorn, H., *Z. Phys. Chem*. 188:45–60 (1995).
7. Smoluchowski, M. V., *Z. Phys. Chem*. 92:129–168 (1917).
8. Seinfeld, J. H., *Atmospheric Chemistry and Physics of Air Pollution*, Wiley, New York, 1986.
9. Frenklach, M., *J. Colloid Interface Sci*. 108:237–242 (1985).
10. Frenklach, M., and Harris, S. J., *J. Colloid Interface Sci*. 118:252–261 (1987).
11. Harris, S. J., and Kennedy, I. M., *Combust. Flame* 78:390–397 (1989).
12. Frenklach, M., and Wang, H., in *Soot Formation in Combustion: Mechanisms and Models* (H. Bockhorn, Ed.), Springer-Verlag, Berlin, 1994, pp. 165–190.
13. Yoshihara, Y., Kazakov, A., Wang, H., and Frenklach, M., *Twenty-Fifth Symposium (International) on Combustion*, The Combustion Institute, Pittsburgh, PA, 1994, pp. 941–948.
14. Bönig, M., Feldermann, C., Jander, H., Lüers, B., Rudolph, G., and Wagner, H. G., *Twenty-Third Symposium (International) on Combustion*, The Combustion Institute, Pittsburgh, 1991, pp. 1581–1587.
15. Feldermann, C., Jander, H., and Wagner, H. G., *Z. Phys. Chem*. 186:127–140 (1994).
16. Fuchs, N. A., *Mechanics of Aerosols*, Pergamon, New York, 1964.
17. Friedlander, S. K., *Smoke, Dust and Haze*, Wiley, New York, 1977.
18. Frenklach, M., in *Numerical Approaches to Combustion Modeling* (E. S. Oran and J. P. Boris, Eds.), American Institute of Astronautics and Aeronautics, Washington, D.C., 1991, pp. 129–154.
19. Harris, S. J., and Kennedy, I. M., *Combust. Sci. Technol*. 59:443–454 (1988).
20. Wang, S. W., and Friedlander, S. K., *J. Colloid Interface Sci*. 24:170–179 (1967).
21. Pratsinis, S. E., *J. Colloid Interface Sci*. 124:416–428 (1988).
22. Mackowski, D. W., Tassopoulos, M., and Rosner, D. E., *Aerosol Sci. Technol*. 20:83–99 (1994).
23. Churchill, S. W., and Usagi, R., *AIChE J*. 18:1121–1128 (1972).
24. Churchill, S. W., and Usagi, R., *Ind. Eng. Chem. Fundam*. 13:39–44 (1974).
25. Mountain, R. D., Mulholland, G. W., and Baum, H., *J. Colloid Interface Sci*. 114:67–81 (1986).
26. Samson, R. J., Mulholland, G. W., and Gentry, J. W., *Langmuir* 3:273–281 (1987).
27. Mountain, R. D., and Mulholland, G. W., *Langmuir* 4:1321–1326 (1988).
28. Mulholland, G. W., Samson, R. J., Mountain, R. D., and Ernst, M. H., *Energy Fuels* 2:481–486 (1988).
29. Zhang, H. X., Sorensen, C. M., Ramer, E. R., Oliver, B. J., and Merklin, J. F., *Langmuir* 4:867–871 (1988).
30. Gangopadhyay, S., Elminyawi, I., and Sorensen, C. M., *Appl. Optics* 30:4859–4864 (1991).
31. Sorensen, C. M., Cai, J., and Lu, N., *Appl. Optics* 31:6547–6557 (1992).

32. Cai, J., Lu, N., and Sorensen, C. M., *J. Colloid Interface Sci*. 171:470–473 (1995).

33. Megaridis, C. M., and Dobbins, R. A., *Combust. Sci. Technol*. 63:153–167 (1989).

34. Megaridis, C. M., and Dobbins, R. A., *Combust. Sci. Technol*. 71:95–109 (1990).

35. Dobbins, R. A., Santoro, R. J., and Semerjian, H. G., *Twenty-Third Symposium (International) on Combustion*, The Combustion Institute, Pittsburgh, 1991, pp. 1525–1532.

36. Dobbins, R. A., and Megaridis, C. M., *Appl. Optics* 30:4747–4754 (1991).

37. Charalampopoulos, T. T., and Chang, H., *Combust. Flame* 87:89–99 (1991).

38. Bonczyk, P. A., and Hall, R. J., *Langmuir* 7:1274–1280 (1991).

39. Köylü, Ü. Ö., and Faeth, G. M., *Combust. Flame* 89:140–156 (1992).

40. Köylü, Ü. Ö., and Faeth, G. M., *J. Heat Transfer* 115:409–417 (1993).

41. Köylü, Ü. Ö., and Faeth, G. M., *J. Heat Transfer* 116:971–979 (1994).

42. Köylü, Ü. Ö., and Faeth, G. M., *J. Heat Transfer* 116:152–159 (1994).

43. Köylü, Ü. Ö., Faeth, G. M., Farias, T. L., and Carvalho, M. G., *Combust. Flame* 100:621–633 (1995).

44. Faeth, G. M., and Köylü, Ü. Ö., *Combust. Sci. Technol*. 108:207–229 (1995).

45. Köylü, Ü. Ö., Xing, Y., and Rosner, D. E., *Langmuir* 11:4848–4854 (1995).

46. Puri, R., Richardson, T. F., Santoro, R. J., and Dobbins, R. A., *Combust. Flame* 92:320–333 (1993).

47. Neimark, A. V., Köylü, Ü. Ö., and Rosner, D. E., *J. Colloid Interface Sci*. 180:590–597 (1996).

48. Jullien, R., and Botet, R., *Aggregation and Fractal Aggregates*, World Scientific, Singapore, 1987.

49. Graham, S. C., *Sixteenth Symposium (International) on Combustion*, The Combustion Institute, Pittsburgh, 1977, pp. 663–669.

50. Prado, G., Jagoda, J., Neoh, K., and Lahaye, *Eighteenth Symposium (International) on Combustion*, The Combustion Institute, Pittsburgh, 1981, pp. 1127–1136.

51. Vemury, S., and Pratsinis, S. E., *J. Aerosol Sci*. 26:175–185 (1995).

52. Rogak, S. N., Flagan, R. C., and Nguyen, H. V., *Aerosol Sci. Technol*. 18:25–47 (1993).

53. Tandon, P., and Rosner, D. E., *Ind. Eng. Chem. Res*. 34:3265–3277 (1995).

54. Kruis, F. E., Kusters, K. A., and Pratsinis, S. E., *Aerosol Sci. Technol*. 19:514–526 (1993).

55. Jullien, R., and Meakin, P., *J. Colloid Interface Sci*. 127:265–272 (1989).

56. Farias, T. L., Köylü, Ü. Ö., and Carvalho, M. G., *J. Quant. Spectrosc. Radiat. Transfer* 55:357–371 (1996).

57. Rosner, D. E., and Tandon, P., *AIChE J*. 40:1167–1182 (1994).

58. This conclusion is based on the results depicted in Figs. 9 and 11 of [57] and the present range of conditions: fractal dimension 1.8, Knudsen number based on primary sphere diameter between 2 and 3, number of aggregate primary particles below 100; and the reaction probabili-

ties of 0.1 for the oxidation by OH and below 10^{-3} for the growth by C_2H_2. Under these conditions, the correction factor is below 20% for OH and immeasurably small for C_2H_2. Taking into account that during the aggregation stage the oxidation rate is less than 30% by the absolute value of the total surface reaction rate, the overall correction factor should not exceed 6% for the flames considered in the present study. Furthermore, as evidenced from the present results and discussion, the impact of this correction on the numerical predictions of soot particle properties for the flames considered should be even lower because the rate of surface reactions decreases as aggregation begins.

59. D'Alessio, A., Di Lorentzo, A., Borghese, A., Beretta, F., and Masi, S., *Sixteenth Symposium (International) on Combustion*, The Combustion Institute, Pittsburgh, 1977, pp. 695–708.

60. Haynes, B. S., Jander, H., and Wagner, H. G., *Ber. Bunsenges. Phys. Chem*. 84:585–592 (1980).

61. Penndorf, R. B., *J. Optical Soc. Am*. 52:896–904 (1962).

62. van de Hulst, H. C., *Light Scattering by Small Particles*, Dover, New York, 1981.

63. Bohren, C. F., and Huffman, D. R., *Absorption and Scattering of Light by Small Particles*, Wiley, New York, 1983.

64. Jander, H., personal communication, 1995.

65. Smyth, K. C., and Shaddix, C. R., *Combust. Flame* 107:314–320 (1996).

66. Megaridis, C. M., and Dobbins, R. A., *Aerosol. Sci. Technol*. 12:240–255 (1990).

67. Kee, R. J., Grgar, J. F., Smooke, M. D., and Miller, J. A., Sandia National Laboratories Report No. SAND85-8240, 1985.

68. Frenklach, M., *Chem. Eng. Sci*. 40:1843–1849 (1985).

69. Perry, R. H., and Chilton, C. H., Eds., *Chemical Engineer's Handbook*, McGraw-Hill, New York, 1973.

70. Bird, R. B., Stewart, W. E., and Lightfoot, E. N., *Transport Phenomena*, Wiley, New York, 1960.

71. Kee, R. J., Dixon-Lewis, G., Warnatz, J., Coltrin, M. E., and Miller, J. A., Sandia National Laboratories Report No. SAND86-8246, 1986.

72. Wang, H., and Frenklach, M., *Combust. Flame* 110:173–221 (1997).

73. Frenklach, M., *Twenty-Sixth Symposium (International) on Combustion*, The Combustion Institute, Pittsburgh, 1996, pp. 2285–2293.

74. Hanisch, H., Jander, H., Pape, T., and Wagner, H. G., *Twenty-Fifth Symposium (International) on Combustion*, The Combustion Institute, Pittsburgh, 1995, pp. 577–584.

75. Nyeki, S., and Colbeck, I., *J. Aerosol Sci*. 25:S403–S404 (1994).

76. D'Alessio, A., in *Particulate Carbon: Formation During Combustion* (D. C. Siegla and G. W. Smith, Eds.), Plenum, New York, 1981, pp. 207–256.

77. Jander, H., Petereit, N., and Razus, D. M., *Z. Phys. Chem*. 188:159–175 (1995).

78. Wolfram, S., *Mathematica: A System for Doing Mathematics by Computer*, Addison-Wesley, Reading, MA, 1993.